Angular distribution of ejected electrons from autoionizing 3*pns* states of magnesium

M. D. Lindsay, L.-T. Cai, G. W. Schinn,* C.-J. Dai, and T. F. Gallagher
Department of Physics, University of Virginia, Charlottesville, Virginia 22901
(Received 5 August 1991)

We have measured the angular distribution of electrons ejected from doubly excited autoionizing Rydberg $3pns$ $J=1$ states of magnesium, where $n=10-20$. Two dye lasers cross an atomic beam and excite $3sns\,^1S_0$ states of Mg. A third linearly polarized laser excites the $3pns$ states. The angular distribution is of the form $(\sigma/4\pi)[1+\beta P_2(\cos\theta)]$. We measure β as a function of the energy of the third laser. The β parameter varies over its full range of values, -1 to 2. Our data agree quite well with the predictions of the reaction-matrix–multichannel-quantum-defect theory.

PACS number(s): 34.50.Lf, 32.80.Rm, 32.80.Dz, 82.50.Fv

INTRODUCTION

Recent studies [1,2] have shown that the measured line shapes of resonances in the doubly excited autoionizing Rydberg $3pns$ and $3pnd$ states of Mg are in excellent agreement with the predictions of multichannel-quantum-defect theory (MQDT). MQDT [3] is especially well suited to provide calculated spectra for these states of Mg since it describes a distant electron scattered from a core. In our case the ns electron is scattered from the Mg^+3p excited core. The inner core electron's energy, when transferred to the outer electron, is enough to ionize it. MQDT, within its approximations, provides the wave function of the outgoing electron. In principle, all features of the transition to the $3pns$ state as well as of the final state after autoionization can be calculated.

A number of measurements and MQDT calculations of the line shapes of transitions to autoionizing Rydberg states of alkaline-earth atoms have been made. For example, Mg [1,2], Ca [4,5], Sr [6,7], and Ba [8,9] have all been studied, and in most cases, quite good agreement was found between experiment and theory. In this paper we focus on angular distributions rather than line shapes; specifically, we report measurements of the angular distributions of the electrons from the autoionizing $3pns$ $J=1$ states of Mg, where $n=10-20$. The angular distribution is a much more sensitive test of MQDT than is the line shape of a transition. As we will show later, the angular distribution depends very strongly on excitation amplitudes and phases of the possible $J=1$ channels. In contrast to the angular distributions, the line shapes for the $3sns\rightarrow 3pns$ transition are less complex as they depend on the excitation amplitudes of the small subset of channels which are directly excited. Any errors in the theory have a much greater impact on angular distribution predictions.

Measurements of angular distributions of electrons ejected from alkaline-earth elements in analogous doubly excited autoionizing Rydberg states of Ca, Sr, and Ba have been performed previously [5,7,9]. Mg is significantly different from these similar but heavier atoms for two reasons. It has a very small fine-structure splitting of its ion $3p$ level. The $Mg^+3p_{J=1/2}-3p_{J=3/2}$ fine-structure splitting is only 92 cm^{-1}, compared to 223, 801, and 1691 cm^{-1} for the analogous levels of Ca^+, Sr^+, and Ba^+. Since the natural linewidths of the Mg $3sns\rightarrow 3pns$ transitions for $n\sim 15$ are of the order of 92 cm^{-1}, transitions to both fine-structure levels overlap and interfere to a much greater extent than do those of Ca, Sr, or Ba. Also, unlike Ca, Sr, and Ba, the $3pns$ state of Mg cannot autoionize to a lower energy d state of the ion. Thus there are fewer final states for the autoionizing Mg $3pns$ states, relative to their Ca, Sr, or Ba analogs. The first reason tends to make the spectra more complex; the second tends to make it less complex. Overall, the spectra and angular distribution of the Mg states are fairly complex.

EXPERIMENT

Our apparatus, shown in Fig. 1, had three dye laser oscillators and amplifiers, pumped by a pulsed Nd:YAG

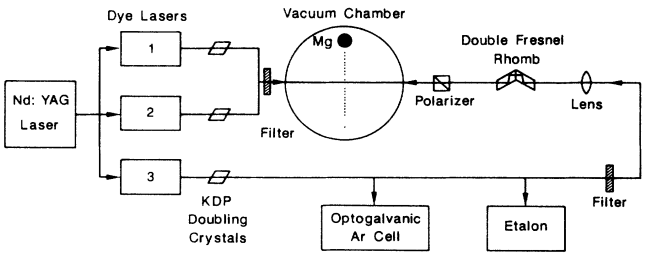

FIG. 1. Schematic diagram of the optical apparatus. Each dye laser is a combination of oscillator and amplifier. The doubling crystals are angle tuned; the crystal for the third laser is mounted in a servo-feedback loop so that it tracks the tuning of the third laser. The filters block visible and ir light and only pass uv light. The optogalvanic Ar cell provides absolute frequency reference markers for the third laser. The étalon provides regularly spaced fringes for linearizing the scan of the third laser. Both the Ar cell and the étalon use undoubled light. The double Fresnel rhomb rotates the linear polarization of the third laser, which allows the detectors to measure different points in the angular distributions. The axis of rotation of the rhomb is the laser beam itself. The linear polarizer ensures that the third laser beam is, in fact, linearly polarized. It is rotated to match the setting of the rhomb.

laser (where YAG denotes yttrium aluminum garnet) operating at 20 Hz. The dye laser pulses had a pulse width of about 5 ns and a frequency width of about 1 cm^{-1}. Each laser beam was frequency doubled to the near uv in potassium dihydrogen phosphate doubling crystals. The three collinear beams crossed a collimated thermal atomic beam of Mg at right angles in a vacuum chamber at a pressure of 5×10^{-6} Torr.

We set the first laser to the $3s3s\ ^1S_0 \rightarrow 3s3p\ ^1P_1$ transition of Mg at 285 nm ($3s3s$ being the ground state). The second laser was tuned to various transitions $3s3p\ ^1P_1 \rightarrow 3sns\ ^1S_0$, where $n=10$–20. Its frequency-doubled wavelength was in the range 375–400 nm. These first two lasers were used solely to prepare the singly excited, Rydberg, $3sns$ Mg atoms. The third dye laser was used to excite the inner $3s$ electron of the now isolated Mg^+ core to the $3p$ level, while leaving the outer ns electron's orbit relatively unchanged. This method is known as "isolated core excitation" [10]. We tuned the third laser over a range of $\sim$700 cm^{-1} centered on the peaks of the $3sns \rightarrow 3pns$ transition, and measured the angular distribution as a function of the energy of the third laser. The energy levels of our excitation scheme are shown in Fig. 2.

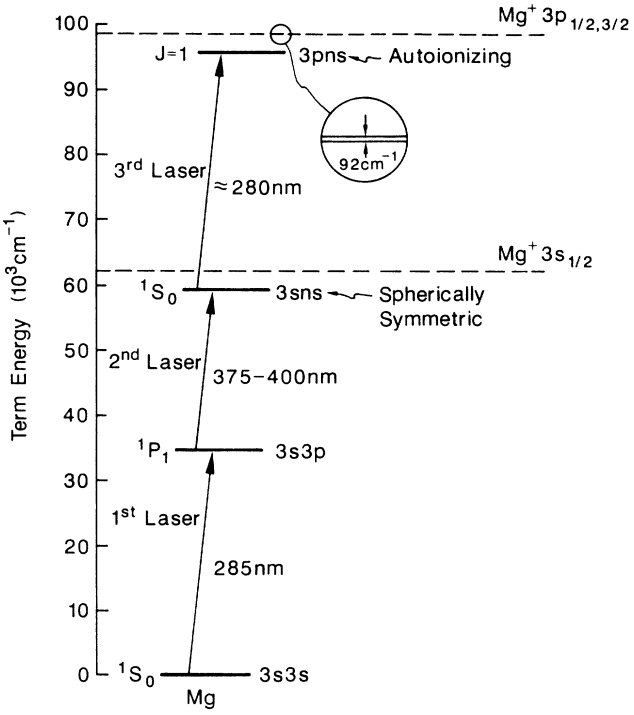

FIG. 2. Energy-level diagram for the three-laser excitation of the $3pns$ states of Mg. The first laser is fixed in frequency and excites the "outer" electron. The second laser is set to excite that electron to a Rydberg state, with a particular n value in the range 10–20. The third linearly polarized laser excites the "inner" electron, and is tuned over a 700-cm^{-1}-wide region centered on the autoionizing $3pns$ resonances. The β parameter, or angular distribution, and line shape of the transition are measured as a function of the tuning of the third laser. The $3pns$ states are split by the fine-structure splitting of the excited ion core. Since the $3sns$ state is spherically symmetric, the angular distribution of the emitted electron is given by $(\sigma/4\pi)[1+\beta P_2(\cos\theta)]$.

A portion of the undoubled third laser beam was split off and fed to an Ar optogalvanic cell which provided an absolute frequency calibration. Another portion was sent through an étalon, producing fringes 4 cm^{-1} apart, providing a means for linearizing the third laser scan.

The main portion of the third laser went through a double Fresnel rhomb and separate linear polarizer before striking the Mg beam. The Fresnel rhomb allowed rotation of the linear polarization of the beam without loss of intensity. Putting the linear polarizer next to last in the chain of optical elements maximized the polarization purity of the third laser beam. The vacuum chamber windows were the last optical elements the laser beams passed through before striking the Mg beam. The windows, selected for their lack of birefringence, were of uv-grade fused silica. After passing through the entire optical chain (while the chamber was under vacuum) the third laser beam's ratio of intensity of the desired polarization to intensity of the orthogonal polarization was at least 100:1.

To measure angular distributions, we used two independent electron detectors to detect electrons ejected from the autoionizing Mg atoms. Each consisted of a pair of microchannel plates (MCP's) in a telescopic arrangement. Each pair of MCP's amplified the electron pulses by $\sim10^8$. The stack of MCP's was mounted at the back of a 10-cm-long time-of-flight tube, to provide energy analysis. The distance from the laser–atomic-beam interaction point to the MCP's was about 10 cm. The autoionized electrons produced fast pulses from the MCP's several hundreds of nanoseconds after the laser pulses, the exact timing depending on the kinetic energy of the electrons. Electrons from the three-step excitation arrived first. A weaker signal from Mg ionized by absorbing two 285-nm photons from the first laser arrived about 20 ns later, since those electrons have less energy, as shown in Fig. 2. We could easily temporally resolve the two pulses, and the second pulse was eliminated entirely from the measurements using gated integrators which closed well before the second pulse arrived.

Figure 3 is a schematic diagram of the electronics used to process the signals. Each signal path was independent, and steps were taken to minimize any coupling of signals between the paths. Fast amplifiers immediately amplified the signals when they exited the vacuum chamber. Gated integrators, triggered by the laser pulses with an appropriate delay, converted the signals to slowly varying dc levels. The gates were 6 ns long. We averaged the signals using exponential averaging with a time constant of 0.5 s, which corresponded to 10 shots of the lasers. At the scan rates we used, this averaging produced a 0.4-cm^{-1} averaging of the spectra. The averagers' outputs were recorded by the analog-to-digital converter (ADC) and computer every 0.3 s. The ADC also simultaneously recorded étalon fringes and Ar lines produced by the third laser. Later during data analysis the data files' horizontal axes were adjusted to force a uniform spacing between the étalon fringes, thereby linearizing the scans. The horizontal axes were transformed using the positions

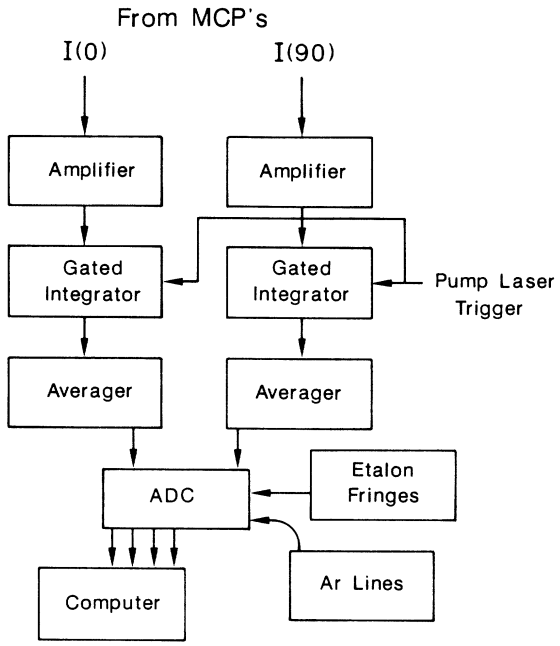

FIG. 3. Schematic of signal path and electronics. Fast weak pulses come from the multichannel plates (MCP's) and are amplified and gated. The gates are 6 ns long, synchronized with the laser pulses. Each signal is averaged over ten shots of the laser, and then recorded by the computer. Each data channel is independent. Also recorded simultaneously are the Ar lines and etalon fringes for use in the data analysis.

of strong Ar lines, to put them on an absolute scale [11].

For data taking the polarization (electric-field vector) of the third laser was set to point straight into one of the electron detectors. The direction of polarization of the third laser is defined $\theta=0$, and that detector measured the $I(0)$ signal. The two detectors were set at 90° to each other, with respect to the laser–atomic-beam interaction point, so the other detector measured $I(90°)$. The two detectors and the laser–atomic-beam interaction point were in a plane perpendicular to the direction of propagation of the third laser. The advantages of this geometry will be discussed in the following section. The area of the MCP detectors subtended a nonzero solid angle; however, for our geometry this produced a 1% error at most in measuring the β parameter, an error well below our experimental uncertainty. Consequently, we ignored the nonzero solid angle of the detectors. We sprayed the entire inside of the detector arrangement with graphite powder, and surrounded the region with two layers of μ metal to reduce stray static electric and magnetic fields which might alter the path of the electrons and distort the angular distributions.

The very high peak power of pulsed lasers allowed us to saturate the three transitions. In particular, the important $3sns \rightarrow 3pns$ third transition was strongly depletion broadened [12]. This broadening was homogeneous and was the same for Mg atoms ejecting electrons at $\theta=0$ or 90°. The asymmetry parameter β depends only on the ratio $I(0)/I(90)$, as seen below, so depletion broadening had no effect on the β spectrum. Uncertainties were decreased by having the maximum possible signal, so we saturated our transitions to the extent possible to get good signals in the outlying wings of the line shapes.

The angular distribution is defined with respect to θ, the polar angle of the direction in which the autoionized electron is ejected as measured from the direction of polarization of the third laser. Since the $3sns\ ^1S_0$ states which absorb the last laser photon and eject an electron are spherically symmetric, a theorem of Yang [13] states that the angular distribution $I(\theta)$ must be of the form

$$\frac{d\sigma}{d\Omega}(\theta)\equiv I(\theta)=\frac{\sigma}{4\pi}[1+\beta P_2(\cos\theta)]\ , \tag{1}$$

where σ is the total cross section, $P_2(x)$ is the second Legendre polynomial $(3x^2-1)/2$, and β is a number $-1\leq\beta\leq 2$. This result is based upon general symmetry arguments and the assumption of electric dipole excitation of a spherically symmetric initial state. The β parameter gives the amount of deviation from a spherically symmetric distribution: if $\beta=0$, then $I(\theta)$ is spherical. If $\beta=2$ or -1, then $I(\theta)\propto\cos^2(\theta)$ or $\sin^2(\theta)$, respectively.

Taking advantage of this relatively simple form of $I(\theta)$, we measured the angular distribution by measuring only $I(0)$ and $I(90°)$. Figure 4 shows $I(0)$ and $I(90)$, [with $I(90)$ multiplied by a factor of 20] for a scan of the transition to the $3p\,11s$ state. One can easily see that $I(0)$ and $I(90)$ are not at all proportional to one another, indicating a varying β parameter. Setting $\theta=0$, and then

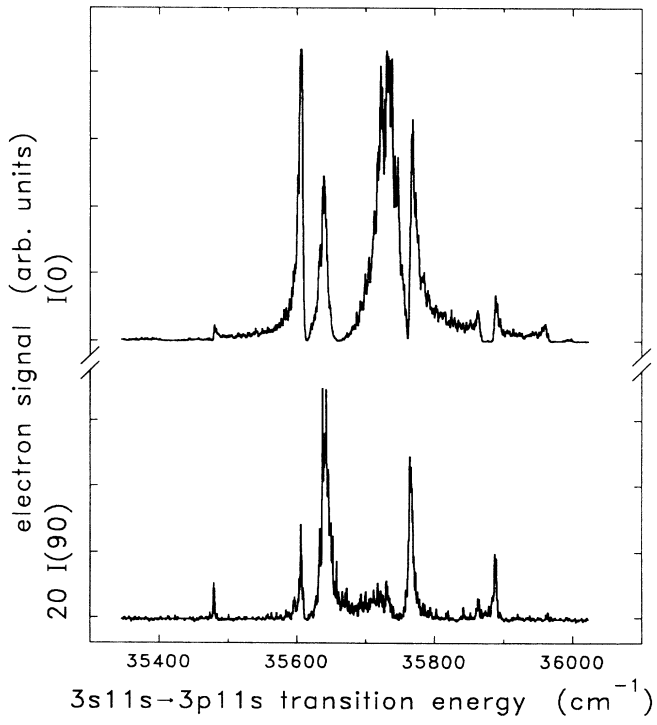

FIG. 4. Line shapes of the electron signal for the $3s11s\rightarrow 3p11s$ transition, detected simultaneously at two different angles θ. The top trace is $I(\theta=0)$, and the bottom is $I(\theta=90°)$ multiplied by a factor of 20. $I(0)$ and $I(90)$ are used to derive the β parameter according to Eq. (3).

$\theta=90°$ in Eq. (1), and taking the ratio, we have

$$\frac{I(0)}{I(90)}=\frac{1+\beta}{1-\beta/2} . \tag{2}$$

Solving for β, we find

$$\beta=\frac{2\frac{I(0)}{I(90)}-2}{\frac{I(0)}{I(90)}+2} . \tag{3}$$

Using this scheme we measured β on a continuous basis as the third laser was tuned smoothly. We tested Eq. (3) by measuring the signal in one detector and rotating the laser polarization with a fixed laser frequency. The resulting angular distribution agreed well with Eq. (1), and a fit to Eq. (1) gave a β that agreed well with the β derived from Eq. (3) using both detectors, at the same laser frequency. Figure 5 shows the angular distribution at fixed laser frequency as a function of θ, and the least-squares fit to Eq. (1), which yields $\beta=1.8$ for this distribution.

To correct for the different overall efficiency of each detector and associated electronics, we set the laser polarization to point midway between the two detectors. Then the two signals must be the same by symmetry, regardless of the value of β. This gave a correction factor which we used to correct for the difference in the detectors' efficiencies. We did this correction for every two data scans. Tests were also made to verify consistency of the data when the $I(0)$ and $I(90)$ detectors were exchanged.

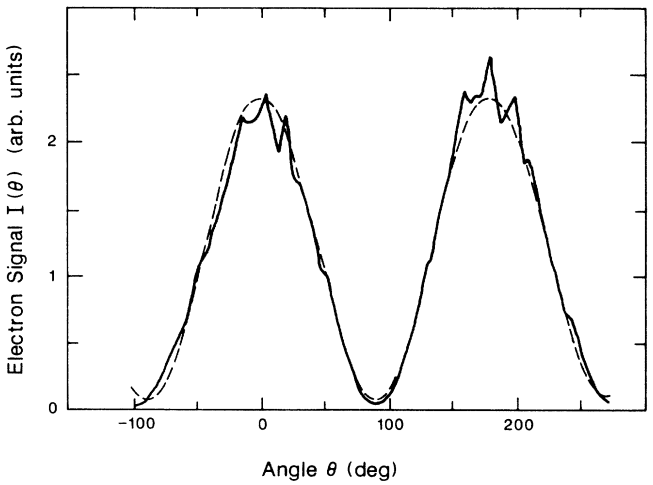

FIG. 5. Angular distribution of the electron current for the $3s13s\rightarrow 3p13s$ transition, with the third laser set to 35 755 cm^{-1}. This is the graph of the signal from one detector, as the laser polarization is rotated under it. All laser frequencies are fixed for these data. The solid line shows the data, and the dashed line is a fit of the theoretically predicted form $(\sigma/4\pi)[1+\beta P_2(\cos\theta)]$ to the data. The fit shows that $\beta=1.8$ for these data. This is the same β obtained using both detectors and Eq. (3) of the text (with the laser set to the same energy). Both methods for measuring β give the same results, demonstrating that the β parameter and angular distribution can be found by measuring the electron signal at only two angles, $\theta=0°$ and 90°.

We verified that the angular distributions $I(\theta)$ were periodic with a period of 180°. We also checked that the factor obtained to correct for the two detectors' difference in efficiency was the same for the laser polarization pointing to +45°, or to −45°.

To obtain an additional verification that our electron signals were linearly proportional to the number of electrons ejected, and that the angular distributions derived from them were undistorted, we altered one of the electron detectors to detect the Mg^+ ions produced by autoionization. This involved changing the high-voltage po-

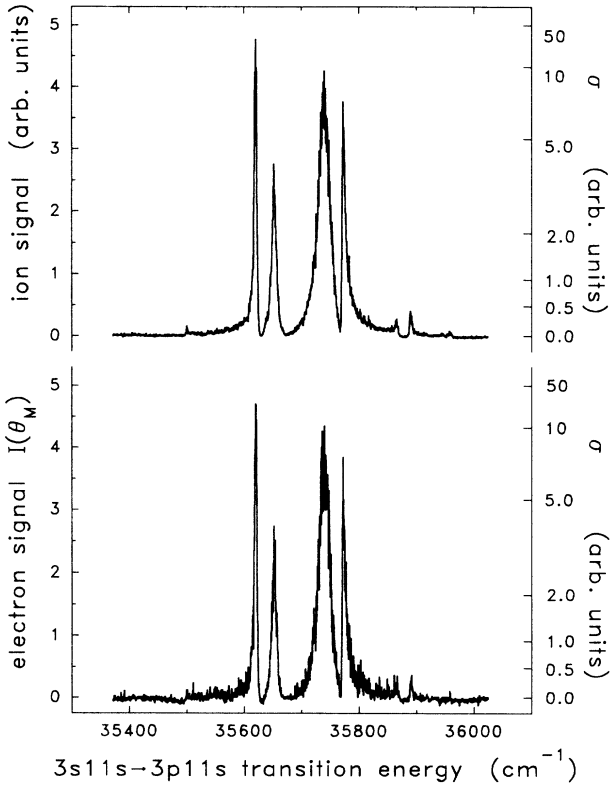

FIG. 6. The line shape of the $3s11s\rightarrow 3p11s$ transition as measured by the electron detector at an angle $\theta=\theta_M=54.7°$ and by the ion detector. The electrons and matching Mg^+ ions are emitted when the $3p11s$ state autoionizes. The ion detector collects ions emitted in all directions, so the ion signal is proportional to σ, the total cross section integrated over all angles. At $\theta=\theta_M$ the wavelength dependence of the electron signal should be that of the ion signal. The two signals, ion and electron, were taken simultaneously. In order to increase signal-to-noise ratio in the wings of the transitions, we depletion broadened, or optically saturated, the transitions. The left vertical scale is the observed signal, proportional to the saturated total cross section σ. As described in the text, we obtained a corresponding nonlinear (nonlogarithmic) scale for the unsaturated total cross section σ shown on the right-hand side of the graph, by comparing our data and the unsaturated MQDT model predictions artificially saturated via Eq. (4). If the right vertical scale and the data graph were stretched vertically so that the right vertical scale was linear, then the data graph would be the unsaturated line shape. The units of the left and right scales are the same, but arbitrary, since all of our cross-section measurements were relative.

larity powering the MCP's in the ion detector, as well as lengthening the gate delay and width of the ion signal gated integrator, since the Mg^+ ions traveled to their detector much more slowly than the electrons did to theirs. Also we placed a pair of mesh plates, suitably coated with graphite powder, around the laser–atomic-beam interaction point, and applied a 100-V/cm fast pulse to it after the lasers were off and the ejected electrons had left the interaction region, to drive the ions to the ion detector. The field was zero when the lasers were on, so the Mg states and the ejected electron trajectories were unperturbed by this arrangement.

Since the 100-V/cm field collected and drove all of the ions to the ion detector regardless of the angle in which they were emitted, the ion signal corresponds to the integral of Eq. (1) over a full sphere. This integral is simply σ, the total cross section. When $\theta=\theta_M\equiv\cos^{-1}(3^{-1/2})=54.7...$ deg, $P_2(\cos\theta)$ is zero; so by Eq. (1) the electron signal $I(\theta=\theta_M)$ should be simply $\sigma/4\pi$ and should be exactly proportional to the ion signal, regardless of what β is at any place in the spectrum. Figure 6 shows an electron signal measured at $\theta=\theta_M$, and the ion signal taken simultaneously. The agreement is excellent.

The line shapes of some of the transitions we measured are shown in Figs. 6–8. These are ion signals that represent the saturated line shapes of the transitions $3sns\rightarrow 3pns$, where $n=11$ for Fig. 6, $n=14$ for Fig. 7, and $n=18$ for Fig. 8. The horizontal axes of Figs. 6 and 7 are the same; that of Fig. 8 covers fewer wave numbers in order to show more clearly the narrower features of the $n=18$ state.

As mentioned previously, the transitions were depletion broadened, or saturated, so our line shapes are not the natural line shapes and are not exactly proportional to the cross section σ. The exact amount of saturation varied from scan to scan depending on the power output of the lasers. We have modeled the saturation using [12]

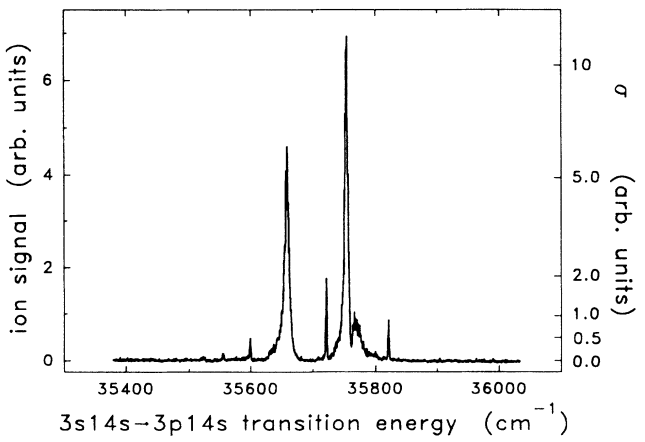

FIG. 7. The line shape of the $3s14s\rightarrow 3p14s$ transition as measured by the ion detector. The comments for Fig. 6 apply to this graph also.

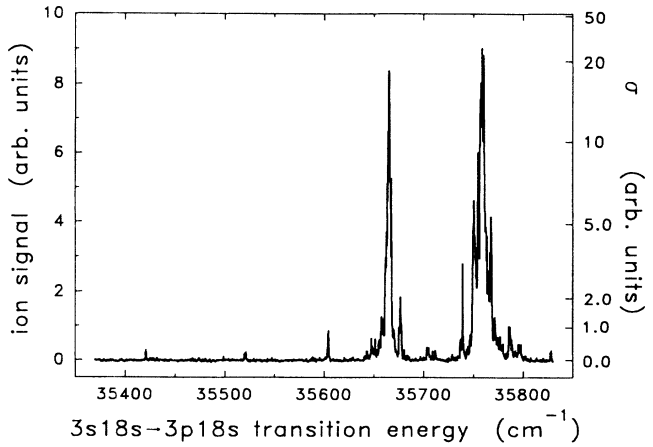

FIG. 8. The line shape of the $3s18s\rightarrow 3p18s$ transition as measured by the ion detector. The comments for Fig. 6 apply to this graph also. The horizontal axes of Figs. 6 and 7 are the same. The horizontal axis of this graph has the same left end point as Fig. 6, but runs only to 35 800 cm^{-1}, in order to better show the narrower features of the higher n state spectrum.

$$I=I_0[1-\exp(-\sigma\Phi)]\ , \tag{4}$$

where I is the observed signal intensity we measured, σ is the underlying unsaturated line shape, and Φ is proportional to the laser flux. Φ functions as a saturation parameter. In addition to predicting the β parameter, the model described in the following section predicts the unsaturated line shapes of transitions. We artificially saturated the model line shapes using a range of values for Φ, and then selected the Φ which gave the best agreement between the saturated model line shape and the data. For Fig. 6 we used $\Phi=0.2$; for Figs. 7 and 8 we used $\Phi=0.1$. The artificially saturated theory line shapes agreed fairly well with our measured line shapes. We normalized the linear vertical scale of each of the measured line shapes so that they matched the corresponding artificially saturated model line shape. This gave the linear scales on the left-hand sides of Figs. 6–8. Then we used Eq. (4) to derive the nonlinear scale on the right-hand sides of Figs. 6–8 from the linear scale for each graph. The nonlinear scales show the underlying unsaturated cross section σ for the transitions, i.e., what the signal would be (in the same units as the linear scale) in the absence of saturation. By reducing the power of the third laser, we were able to measure unsaturated line shapes of our transitions, and the agreement with unmodified theoretical line shapes was quite good, even better than that described in Ref. [2]. If the lines are unsaturated, the signal itself in the wings of the lines is so small that the β parameter cannot be determined reliably. We show these saturated line shapes since they were what we actually used to calculate the β parameter spectra, and so are more pertinent to this paper, although they are more difficult to compare directly with theory. Also, the Mg transition line shapes (but not the β parameters) have already been reported [2], although with lower signal-to-noise ratio and over a smaller tuning range.

THEORY

In this section we summarize the derivation of the β parameter from the MQDT reaction, or $\underline{R}$ or $\underline{K}$, matrix provided to us by Greene [14,2]. In the autoionization of a $3pns$ state the initially bound ns Rydberg electron scatters from the $3p$ Mg^+ core, energy is transferred from the core to the electron, and the electron is ejected. All of the autoionizing states we measured were $J=1$. The relevant jj- and LS-coupled ϕ_i and ψ_i $J=1$ Mg channels are listed in the following:

$$\begin{bmatrix}\phi_1\\ \phi_2\\ \phi_3\\ \phi_4\\ \phi_5\\ \phi_6\\ \phi_7\end{bmatrix} = \begin{bmatrix}3s_{1/2}\epsilon p_{1/2}\\ 3s_{1/2}\epsilon p_{3/2}\\ 3p_{1/2}ns_{1/2}\\ 3p_{3/2}ns_{1/2}\\ 3p_{1/2}nd_{3/2}\\ 3p_{3/2}nd_{3/2}\\ 3p_{3/2}nd_{5/2}\end{bmatrix} = \underline{V} \begin{bmatrix}\psi_1\\ \psi_2\\ \psi_3\\ \psi_4\\ \psi_5\\ \psi_6\\ \psi_7\end{bmatrix} = \begin{bmatrix} (\frac{1}{3})^{1/2} & 0 & 0 & (\frac{2}{3})^{1/2} & 0 & 0 & 0\\ (\frac{2}{3})^{1/2} & 0 & 0 & -(\frac{1}{3})^{1/2} & 0 & 0 & 0\\ 0 & -(\frac{1}{3})^{1/2} & 0 & 0 & (\frac{2}{3})^{1/2} & 0 & 0\\ 0 & (\frac{2}{3})^{1/2} & 0 & 0 & (\frac{1}{3})^{1/2} & 0 & 0\\ 0 & 0 & (\frac{1}{3})^{1/2} & 0 & 0 & (\frac{1}{6})^{1/2} & (\frac{1}{2})^{1/2}\\ 0 & 0 & (\frac{1}{15})^{1/2} & 0 & 0 & (\frac{8}{15})^{1/2} & -(\frac{2}{5})^{1/2}\\ 0 & 0 & (\frac{3}{5})^{1/2} & 0 & 0 & -(\frac{3}{10})^{1/2} & -(\frac{1}{10})^{1/2}\end{bmatrix} \begin{bmatrix}3s\epsilon p\ ^1P\\ 3pns\ ^1P\\ 3pnd\ ^1P\\ 3s\epsilon p\ ^3P\\ 3pns\ ^3P\\ 3pnd\ ^3P\\ 3pnd\ ^3D\end{bmatrix} . \tag{5}$$

They are related by the orthogonal transformation matrix $\underline{V}$.

The first two jj channels are open, indicating the outer electron is in a true continuum state for them, and the other jj channels are closed. The open eigenchannels are labeled by ρ: $\rho=1,2$. There are two autoionization eigenchannels:

$$\Psi^{(\rho)}=\sum_{i=1}^{7} A_i^{(\rho)}|\phi_i\rangle=\sum_{\alpha=1}^{7} B_\alpha^{(\rho)}|\psi_\alpha\rangle,\quad \rho=1,2 . \tag{6}$$

The A_i's or B_α's, derived from the $\underline{K}$ matrix, determine the contribution of each jj or LS channel to each collision eigenstate $\Psi^{(\rho)}$.

The $\underline{K}$ matrix [14] we use is the same as that in Ref. [2], p. 2317. The elements of the matrix are slowly varying functions of energy and are given at three energies. Interpolation is used to obtain a $\underline{K}$ matrix at all the energies we need. The matrix is provided in LS-coupled form; we transform it to jj-coupled form using the transformation matrix $\underline{V}$ of Eq. (5):

$$\underline{K}^{jj}=\underline{V}\,\underline{K}^{LS}\underline{V}^T . \tag{7}$$

$\underline{K}^{jj}$ must be diagonalized. Its eigenvalues $\tan(\pi\mu_\alpha)$ are given by

$$\underline{K}^{jj}=\underline{U}(\tan\pi\mu)\underline{U}^T , \tag{8a}$$

which is written term by term as

$$(K^{jj})_{ij}=\sum_\alpha U_{i\alpha}\tan\pi\mu_\alpha(U^T_{\alpha j}) . \tag{8b}$$

$\underline{U}$ is the unitary transformation diagonalizing the jj coupled $\underline{K}$ matrix. The $|\phi_i\rangle$ satisfy $r=\infty$ boundary conditions, and the $|\psi_\alpha\rangle$ satisfy $r=0$ boundary conditions. These boundary conditions lead to [15]

$$\sum_\alpha U_{i\alpha}\sin[\pi(\nu_i+\mu_\alpha)]B_\alpha^{(\rho)}=0 \tag{9a}$$

and

$$\sum_\alpha U_{i\alpha}\cos[\pi(\nu_i+\mu_\alpha)]B_\alpha^{(\rho)}=A_i^{(\rho)} . \tag{9b}$$

$U_{i\alpha}$ and μ_α are obtained from the $\underline{K}$ matrix via Eq. (8b). A nonzero solution exists if

$$\det\{U_{i\alpha}\sin[\pi(\nu_i+\mu_\alpha)]\}=0 . \tag{10}$$

In Eqs. (10), (9a), and (9b) ν_i is the effective quantum number of the i^{th} jj channel. In this case

$$\nu_3=\nu_5=\left[\frac{\mathcal{R}}{E_{\text{IP}1/2}-E}\right]^{1/2} \tag{11a}$$

and

$$\nu_4=\nu_6=\nu_7=\left[\frac{\mathcal{R}}{E_{\text{IP}3/2}-E}\right]^{1/2} , \tag{11b}$$

where $\mathcal{R}$ is the Rydberg constant for Mg, 109 734.86 cm^{-1}, and E is the energy of the autoionizing state in cm^{-1} above the ground state (i.e., E is the sum of energies of the three laser photons). The first laser photon energy is 35 051.36 cm^{-1}. The second laser photon energy is given for each n by Ref. [2]. The $E_{\text{IP}J_c'}$ are the Mg^+ $3p_{1/2}$ and $3p_{3/2}$ ionization limits, which are 97 340.33 and 97 431.90 cm^{-1}, respectively. (J_c' is the total angular momentum of the excited ion core.) ν_i is in general not an integer.

In Eq. (10), ν_1 and ν_2 are both replaced by $-\tau_1$, and then by $-\tau_2$, giving two versions of Eq. (10). Explicitly, Eq. (10) becomes

$$\begin{vmatrix} U_{11}\sin\pi(-\tau_\rho+\mu_1) & U_{12}\sin\pi(-\tau_\rho+\mu_2) & U_{13}\sin\pi(-\tau_\rho+\mu_3) & \cdots & U_{17}\sin\pi(-\tau_\rho+\mu_7) \\ U_{21}\sin\pi(-\tau_\rho+\mu_1) & U_{22}\sin\pi(-\tau_\rho+\mu_2) & U_{23}\sin\pi(-\tau_\rho+\mu_3) & \cdots & U_{27}\sin\pi(-\tau_\rho+\mu_7) \\ U_{31}\sin\pi(\nu_3+\mu_1) & U_{32}\sin\pi(\nu_3+\mu_2) & U_{33}\sin\pi(\nu_3+\mu_3) & \cdots & U_{37}\sin\pi(\nu_3+\mu_7) \\ . & . & . & \cdots & . \\ . & . & . & \cdots & . \\ . & . & . & \cdots & . \\ U_{71}\sin\pi(\nu_7+\mu_1) & . & . & \cdots & U_{77}\sin\pi(\nu_7+\mu_7) \end{vmatrix} = 0 , \quad (10')$$

where $\rho=1,2$. In Eq. (10') $-\pi\tau_\rho$ is the highly energy-dependent continuum phase of the collision eigenstate $\Psi^{(\rho)}$. Each τ_ρ is obtained by solving Eq. (10') at each energy. The variations in τ_ρ are due to resonances in the MQDT core scattering process. The number of independent τ's is the same as the number of open channels. For example, if the excitation energy were above 97 340.33 cm^{-1}, there would be four open channels, four τ's, four $\Psi^{(\rho)}$'s, and ρ would equal 1–4. All of our excitations were at energies below the Mg^+ $3p_{1/2}$ limit.

For each ρ at each energy, Eq. (9a), with both ν_1 and ν_2 replaced by $-\tau_\rho$, is used to find the $B_i^{(\rho)}$. Then the $A_i^{(\rho)}$'s, as a function of energy E, are given by Eq. (9b). Following angular-momentum-transfer theory [16] we use the $A_i^{(\rho)}$'s to calculate β as a function of E. Starting from the bound $3sns$ state, the basic reaction is

$$Mg(\mathbf{J}_0,\pi_0)+\gamma(\mathbf{J}_\gamma,\pi_\gamma)\rightarrow Mg^+(\mathbf{J}_c,\pi_c)+e^-(\boldsymbol{l},\mathbf{s},\pi_e) . \quad (12)$$

Here $\mathbf{J}$ is the total angular momentum. J_0 and π_0 are the angular momentum and parity of the initial Mg $3sns$ $^1S_0$ state. γ refers to the third laser photon; $\mathbf{J}_\gamma$ and π_γ are the angular momentum and parity of the photon. $\mathbf{J}_c$ and π_c are the angular momentum and parity of the residual ion core. $\boldsymbol{l}$ and $\mathbf{s}$ are the orbital angular momentum and spin of the ejected electron; π_e is its parity. The orbital angular momentum and spin of the inner electron make up $\mathbf{J}_c$. Π is the parity; $\pi_0=1$, $\pi_\gamma=-1$, $\pi_c=1$, and $\pi_e=(-1)^l$. Conservation of angular momentum and parity gives us

$$\mathbf{J}=\mathbf{J}_0+\mathbf{J}_\gamma=\mathbf{J}_c+\mathbf{s}+\boldsymbol{l}=\mathbf{J}_{cs}+\boldsymbol{l} \quad (13)$$

and

$$\Pi=\pi_0\pi_\gamma=\pi_c(-1)^l . \quad (14)$$

We measure only $J=1$ final states in this experiment. For our case, the only ion core state available is $3s_{1/2}$, so $J_c=\frac{1}{2}$. Of course $s=\frac{1}{2}$. Equation (13) then restricts l to be 0, 1, or 2. Equation (14) further restricts l to be 1, so we always have an outgoing p wave electron. $\mathbf{J}_{cs}=\mathbf{J}_c+\mathbf{s}$ is the outer electron spin coupled with the total core angular momentum, and has the values 0 or 1 in our case.

Angular momentum transferred to the core plus electron spin system is

$$\mathbf{J}_t=\mathbf{J}_{cs}-\mathbf{J}_0=\mathbf{J}_\gamma-\boldsymbol{l} . \quad (15)$$

The reaction processes of Eq. (12) can be divided into two main categories as follows:

$$\pi_0\pi_c=\begin{cases}(-1)^{J_t} & \text{parity favored, no spin flip} \quad (16a)\\ -(-1)^{J_t} & \text{parity unfavored, spin flip} . \quad (16b)\end{cases}$$

Since the atom is initially in a singlet state, in process (16a) the outer electron retains its spin direction, and the final state is still a singlet. In process (16b) the spin flips and a triplet final state results.

The above leads to only two possible values for J_{cs}, 0 or 1. $J_{cs}=0$ indicates a singlet state, and $J_{cs}=1$ indicates a triplet state. Since $J_0=0$, $\mathbf{J}_t=\mathbf{J}_{cs}$ in this special case, and the same singlet-triplet distinction applies to J_t:

$$J_t=\begin{cases}0 & \text{parity favored, singlet} \quad (17a)\\ 1 & \text{parity unfavored, triplet} . \quad (17b)\end{cases}$$

From Refs. [16] and [7] we have β given in terms of scattering matrix elements $S_l(J_t)$:

$$\beta=\frac{2|S_1(0)|^2-3|S_1(1)|^2}{|S_1(0)|^2+3|S_1(1)|^2} , \quad (18)$$

where

$$S_1(0)=\left[\frac{4\pi\alpha\hbar\omega^3}{3c^2}\right]^{1/2} \times\langle(J_cs)J_{cs}=0,l=1,J-\|D\|J_0\rangle \quad (19a)$$

and

$$S_1(1)=\left[\frac{4\pi\alpha\hbar\omega^3}{3c^2}\right]^{1/2}\frac{1}{\sqrt{3}} \times\langle(J_cs)J_{cs}=1,l=1,J-\|D\|J_0\rangle . \quad (19b)$$

The minus sign in Eqs. (19a) and (19b) indicates that the final state is normalized according to incoming wave boundary conditions.

In our special case it happens that J_{cs} coupling is the same as LS coupling, so

$$\begin{bmatrix} |J_{cs}=0 \;\; l \;\; J\rangle \\ |J_{cs}=1 \;\; l \;\; J\rangle \end{bmatrix} = \begin{bmatrix} 3s\epsilon p\ ^1P_1 \\ 3s\epsilon p\ ^3P_1 \end{bmatrix} = \begin{bmatrix} V'_{11} & V'_{12} \\ V'_{21} & V'_{22} \end{bmatrix} \begin{bmatrix} \phi_1 \\ \phi_2 \end{bmatrix} = \begin{bmatrix} (\frac{1}{3})^{1/2} & (\frac{2}{3})^{1/2} \\ (\frac{2}{3})^{1/2} & -(\frac{1}{3})^{1/2} \end{bmatrix} \begin{bmatrix} 3s_{1/2}\epsilon p_{1/2} \\ 3s_{1/2}\epsilon p_{3/2} \end{bmatrix} . \tag{20}$$

$\underline{V}'$ is the transformation matrix between LS and jj coupling and is sub-block of $\underline{V}$ of Eq. (5). The matrix elements of Eqs. (18) and (19) can be written in terms of the $A_i^{(\rho)}$'s using $\sum_\rho |\Psi^{(\rho)}\rangle\langle\Psi^{(\rho)}| = 1$ and Eq. (6). Explicitly,

$$\begin{aligned} \langle (J_c s) J_{cs}=0, l=1, J-\|D\|J_0\rangle &= \sum_{i=1}^{2} V'_{1i}\langle \phi_i - \|D\|J_0\rangle \\ &= \sum_{i=1}^{2} V'_{1i} \sum_{\rho=1}^{2} \langle \phi_i|\Psi^{(\rho)}\rangle\langle\Psi^{(\rho)} - \|D\|J_0\rangle \\ &= \sum_{i=1}^{2}\sum_{\rho=1}^{2} V'_{1i} \sum_{j=1}^{7} \langle \phi_i|\phi_j\rangle A_j^{(\rho)} \sum_{k=1}^{7} A_k^{(\rho)}\langle \phi_k - \|D\|J_0\rangle \\ &= \sum_{i=1}^{2}\sum_{\rho=1}^{2} V'_{1i} A_i^{(\rho)} \sum_{k=3}^{4} A_k^{(\rho)}\langle \phi_k - \|D\|J_0\rangle \\ &= \sum_{i=1}^{2}\sum_{\rho=1}^{2}\sum_{k=3}^{4} V'_{1i} A_i^{(\rho)} A_k^{(\rho)} D_k \ . \end{aligned} \tag{21a}$$

Here $D_k = \langle \phi_k - \|D\|J_0\rangle$. Reading from right to left, the factors in the last form of Eq. (21a) can be understood as follows. D_k is the dipole matrix element connecting the initial bound $3sns$ state to the k^{th} closed channel. $A_k^{(\rho)}$ is the amplitude of the k^{th} channel in the ρ^{th} eigenchannel. Summing $A_k^{(\rho)} D_k$ over k gives the amplitude for excitation of the ρ^{th} eigenchannel. $A_i^{(\rho)}$ is the amplitude of the i^{th} open channel in the ρ^{th} eigenchannel, and is thus the fractional amplitude for decay into the i^{th} open channel. Finally V'_{1i} gives the fraction of the i^{th} channel which is singlet. When all the factors are put together the $J_{cs}=0$ matrix element is the amplitude for the transition from the initial $3sns$ state to the *singlet* $J=1$ continuum. Similarly, the $J_{cs}=1$ matrix element

$$\begin{aligned} &\langle (J_c s) J_{cs}=1, l=1, J-\|D\|J_0\rangle \\ &\qquad = \sum_{i=1}^{2}\sum_{\rho=1}^{2}\sum_{k=3}^{4} V'_{2i} A_i^{(\rho)} A_k^{(\rho)} D_k \end{aligned} \tag{21b}$$

is the amplitude for the transition from the initial state to the *triplet* $J=1$ continuum. D_k is given by the product of an angular-momentum coupling coefficient, a radial integral, an overlap integral, and a phase factor. There are two nonzero value of D_k. Explicitly,

$$\begin{aligned} D_3 &= \langle 3p_{1/2} \nu' s_{1/2}|\mathbf{r}|3s_{1/2}\nu s_{1/2}\rangle e^{i\pi\tau_\rho} \\ &= \langle 3p_{1/2}\nu' s_{1/2}|\mathbf{r}_\Omega|3s_{1/2}\nu s_{1/2}\rangle \\ &\quad \times \langle 3p_{1/2}|r|3s_{1/2}\rangle\langle \nu'_{1/2}|\nu\rangle e^{i\pi\tau_\rho} \\ &= -\tfrac{1}{3} r_{1/2}\langle \nu'_{1/2}|\nu\rangle e^{i\pi\tau_\rho} \ . \end{aligned} \tag{22a}$$

Similarly

$$D_4 = \frac{\sqrt{2}}{3} r_{3/2}\langle \nu'_{3/2}|\nu\rangle e^{i\pi\tau_\rho} \ . \tag{22b}$$

In the last forms of Eqs. (22a) and (22b) the angular factors have been evaluated. The radial matrix elements between excited and final core states are $r_{J'_c} = \langle 3p_{J'_c}|r|3s_{1/2}\rangle$. In the approximation that $r_{1/2}$ and $r_{3/2}$ are the same, they cancel in the final expression for β. The overlap integral is given by [1]

$$\langle \nu'|\nu\rangle = \frac{2(\nu\nu')^2 \sin\pi(\nu'-\nu)}{\nu^{3/2}\pi(\nu'^2-\nu^2)} \ . \tag{23}$$

The phase factor $e^{i\pi\tau_\rho}$ yields incoming wave normalization [τ_ρ comes from solving Eq. (10′)]. Finally, we can rewrite Eq. (18) as

$$\beta = \frac{2|S^{(0)}|^2 - |S^{(1)}|^2}{|S^{(0)}|^2 + |S^{(1)}|^2} \ , \tag{24}$$

where

$$S^{(0)} = \sum_{i=1}^{2}\sum_{\rho=1}^{2}\sum_{k=3}^{4} V'_{1i} A_i^{(\rho)} A_k^{(\rho)} \Omega_k O_k e^{i\pi\tau_\rho} \ ,$$

$$S^{(1)} = \sum_{i=1}^{2}\sum_{\rho=1}^{2}\sum_{k=3}^{4} V'_{2i} A_i^{(\rho)} A_k^{(\rho)} \Omega_k O_k e^{i\pi\tau_\rho} \ ,$$

$$O_3 = \langle \nu'_{1/2}|\nu\rangle, \quad O_4 = \langle \nu'_{3/2}|\nu\rangle, \quad \Omega_3 = -\tfrac{1}{3}, \quad \Omega_4 = \frac{\sqrt{2}}{3} \ .$$

We have written the $S^{(J_{cs})}$ without the radial matrix elements $r_{J'_c}$, since they cancel in the expression for β. Note that $\beta = 2$ if $S^{(1)} = 0$, and $\beta = -1$ if $S^{(0)} = 0$. These are the parity-favored singlet and parity-unfavored triplet cases, respectively.

RESULTS

Our measurements of the β parameter are presented in Figs. 9–11, superimposed on the theoretical predictions which are indicated by the dotted lines. Figure 9 shows the β spectrum obtained for the $3s11s \rightarrow 3p11s$ excitation over a range of $\sim 700\ \text{cm}^{-1}$ centered on the peaks of the

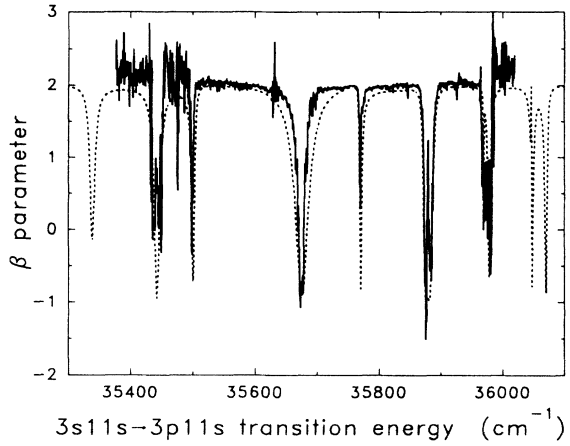

FIG. 9. The β parameter for the $3s11s \rightarrow 3p11s$ transition. The experimental results are shown with the solid line, and the predictions of the $\underline{K}$ matrix–MQDT theory are shown with the dotted line. In some parts of the graph the theoretical prediction is hidden under the data line.

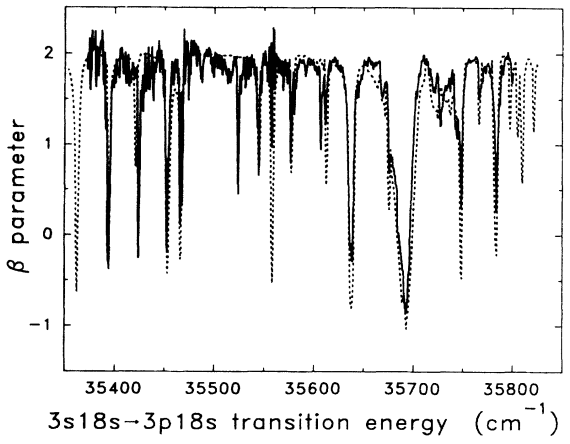

FIG. 11. The caption of Fig. 9 applies except this is the β spectrum of the $3s18s \rightarrow 3p18s$ transition. The horizontal axis of this graph is the same as that of Fig. 8.

transition line shape. Figure 10 shows the β parameter of the $3s14s \rightarrow 3p14s$ transition, and Fig. 11 shows the β parameter of the $3s18s \rightarrow 3p18s$ transition. In each case the theoretical prediction was convolved with the 1-cm^{-1} instrumental linewidth of our measurements, reducing the sharpness of some of the narrow features. The positions of the unperturbed Mg^+ ion transitions $3s_{1/2} \rightarrow 3p_{1/2}$ and $3p_{3/2}$ are located at positions 35 669 and 35 761 cm^{-1}, respectively. For ease of comparison, the horizontal axes of all of our graphs (except Figs. 8 and 11, which correspond to $n=18$) are the same. Although we show only three β spectra, we have measured all of the $3pns$ states, with $n=10$–20. All differ in detail, but show the same general features. We did not measure any states with $n>20$, since starting with $n=20$, the $3s3p \rightarrow 3sns$ and $3s3p \rightarrow 3s(n-1)d$ transitions begin to overlap, and so the $3pns$ and $3p(n-1)d$ states are unavoidably simultaneously excited.

The errors in our measurements of the β parameter vary across the spectra, according to how strong the $I(0)$ or $I(90)$ line shapes were. As shown in Eq. (3) β depends on $I(0)/I(90)$. For the ratio to be correct there must be no signal zero offsets in $I(0)$ or $I(90)$. We carefully readjusted the zero offsets of the signals for each scan. In the worst cases [for the smallest $I(0)$ or $I(90)$], the zero offset error was only 10% of the corresponding signal. If the signal fell below 1000% of the zero offset error, we adjusted the apparatus until the signal was larger again. This limited our measurements to be within ~ 350 cm^{-1} of the line centers. The spectral regions where the zero offset error approached 10% of $I(90)$ were the edges of the spectra, from 35 300 to 35 500 and 35 950 to 36 100 cm^{-1}. In these regions the error in the β parameter is 0.3 or less. For the rest of the spectra, the signals $I(0)$ and $I(90)$ were much stronger, the zero offset error was a much smaller portion of the signal, and $I(0)/I(90)$ was more accurate. For the middle portion of the spectra from 35 500 to 35 950 cm^{-1} the error in β is 0.1 or less. Around the region of 35 600–35 750 cm^{-1}, where the β parameter forms a broad dip to -1 (to be discussed later), the discrepancy between our measurements and theory cannot be accounted for by the experimental error. The horizontal resolution, determined by our laser linewidth, was about 1.5 cm^{-1}.

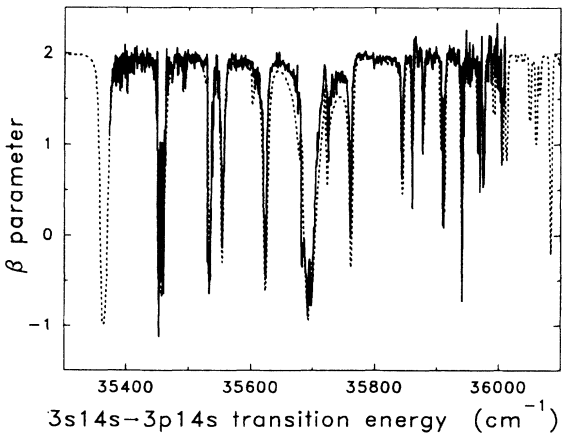

FIG. 10. The caption of Fig. 9 applies except this is the β spectrum of the $3s14s \rightarrow 3p14s$ transition.

Examination of Figs. 9–11 reveals that $\beta \approx 2$ except for relatively sharp deviations. In fact, there are two types of deviations from $\beta=2$. First, more than ~ 100 cm^{-1} from the Mg^+ transitions at 35 669 and 35 761 cm^{-1}, there are narrow deviations from $\beta=2$ at the locations of the autoionizing states. This point is shown by Fig. 12, which displays the theoretically predicted β spectrum and transition line shape, along with $(A_i^{(1)})^2+(A_i^{(2)})^2$, $i=3$–7, from Eq. (6), for the $3p11s$ state. The closed channel A_i "spectra" give the squared amplitudes of each of the jj-coupled closed channels, in other words, they give the locations of the autoionizing $3pns$ and $3pnd$ states. As shown by Fig. 12, away from the Mg^+ resonance lines, all of the deviations from $\beta=2$ coincide with the energies of autoionizing $3pns$ or $3pnd$ states.

The second type of deviation from $\beta=2$ is a broad dip in β to about $\beta=-1$ between the Mg^+ resonance lines.

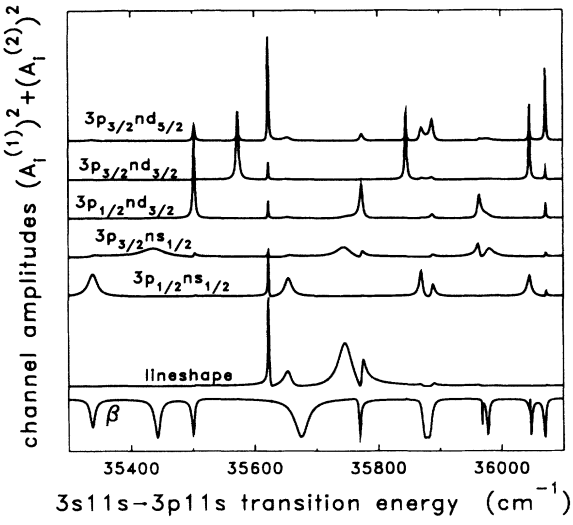

FIG. 12. This purely theoretical graph for the $3s11s \rightarrow 3p11s$ transition shows predictions for (in order from bottom to top) the β parameter, the line shape of the transition, and the amplitudes of the five jj-coupled closed channels, all as a function of the tuning of the third laser. The closed channel graphs are of $(A_i^{(1)})^2+(A_i^{(2)})^2$, where $i=3-7$. In order from bottom to top, they represent the $3p_{1/2}ns_{1/2}$, $3p_{3/2}ns_{1/2}$, $3p_{1/2}nd_{3/2}$, $3p_{3/2}nd_{3/2}$, and $3p_{3/2}nd_{5/2}$ channels. The line-shape graph and the closed channel graphs are each artificially vertically offset from their common minimum value of zero by a different amount so that they will be separated for clarity.

The broad dip is not correlated with the precise locations of autoionizing states. This point can also be seen clearly in Fig. 12 and in the data of Figs. 9–11. Both types of deviation from $\beta=2$ are clearly visible in all of the data we have taken of all of the $3pns$ states, $n=10-20$. As n increases, the narrow dips become narrower, more numerous, and more closely spaced, as one expects since the "interloping" $3pns,d$ autoionizing resonances become more closely spaced at higher n. As n increases the narrow dips in β become superimposed on the broad dip between the Mg^+ transitions; however, the broad dip does *not* become narrower. The numerical explanation for these broad and narrow dips, put in terms of the formulas of Eqs. (21) and (24), is that when β goes to -1, $\langle (J_c s)J_{cs}=0,l=1,J-\|D\|J_0\rangle$ and $|S^{(0)}|$ go to zero, but $\langle (J_c s)J_{cs}=1,l=1,J-\|D\|J_0\rangle$ and $|S^{(1)}|$ do not.

Examining Figs. 9–11 we can see that the $\underline{K}$ matrix calculation reproduces the experimental data almost perfectly. The only real discrepancy is that the broad dip in the β parameter between the Mg^+ resonance lines is often sharper in the experimental data than in the calculated curves, as shown by Figs. 9 and 10. The region around the broad dips is the region of the line-shape peaks where the transition signal is maximum and the measurement error minimum. If one examines only the "shoulders" of the broad dip region of our β spectra near the Mg^+ resonance lines, agreement between theory and our measurements is not always good. The previous study of Ca angular distributions [5] was limited to this region, which may explain their significant discrepancies with the $\underline{K}$ matrix MQDT predictions.

Although the $\underline{K}$ matrix calculation gives excellent values for the β parameter, it is interesting to consider why the β parameter has the form it does. The β spectrum can be divided into two regions: region A, near or between the Mg^+ resonance lines, and region B, which consists of the outer wings of both lines.

The departures of β from 2 are due to two primary reasons. In region B, the β parameter takes on values according to the first of these reasons: If we were photoionizing the $3sns\ ^1S_0$ states directly into the $3s\epsilon p$ continuum, we would expect to excite only the $3s\epsilon p\ ^1P_1$ continuum yielding $\beta=2$. We would expect β to depart from 2 at the locations of autoionizing resonances where the time delay of the resonance would allow the excited state to evolve from the initially excited singlet state to a triplet state before the electron left the atom. When the third laser is tuned to an energy well out in the wings of both Mg^+ resonance lines, we excite both the $3p_{1/2}ns_{1/2}$ and $3p_{3/2}ns_{1/2}$ channels. Since the initial state for the third laser excitation is the $3sns\ ^1S_0$ state, it is reasonable to suppose that we optically excite the coherent superposition of the $3p_{1/2}ns_{1/2}$ and $3p_{3/2}ns_{1/2}$ channels corresponding to the $3pns\ ^1P_1$ channel. The $^1P_1$ superposition naturally scatters directly into the $3s\epsilon p\ ^1P_1$ continuum yielding $\beta=2$. In this case, to excite the singlet state and observe $\beta\sim 2$ requires excitation of the $3p_{1/2}ns_{1/2}$ and $3p_{3/2}ns_{1/2}$ states in roughly the ratio 1:2, since [17]

$$|3pns\ ^1P_1\rangle=-(\tfrac{1}{3})^{1/2}|3p_{1/2}ns_{1/2}\rangle+(\tfrac{2}{3})^{1/2}|3p_{3/2}ns_{1/2}\rangle\ .$$

Also required is minimal time delay between excitation and the ejection of the electron. Both of these conditions are met far from the Mg^+ resonance lines and away from the other $3pns,d$ resonances. However, when one or the other is violated, departures from $\beta=2$ are observed. Far from the Mg^+ resonance lines, in region B, the departures are due to the time delay introduced by autoionizing resonances. The time delay allows effects such as spin-orbit coupling and/or exchange interactions to change the total spin S of the system. The above reason also influences the value of β in region A and produces the narrow dips in the β parameter in both regions A and B.

The second reason occurs in region A, where the third laser is tuned near or between the Mg^+ resonance lines. Here the $3p_{1/2}ns_{1/2}$ and $3p_{3/2}ns_{1/2}$ channels are unlikely to be excited in a ratio 1:2, so an admixture of the $^1P_1$ singlet channel and the $^3P_1$ triplet channel is initially excited. The admixture of singlet and triplet channels scatters into singlet and triplet continua, yielding again departures from $\beta=2$. The above situation apparently only applies to region A of the β spectrum, and leads to the broad dip of the β parameter in that region.

In conclusion we have measured the angular distribution of ejected electrons from autoionizing doubly excited $3pns$ Rydberg states of Mg, where $n=10-20$. As might be anticipated for a case in which there are only two continua, β spans the full range from -1 to 2. Taken as a whole, the measurements are in quite good agreement with the β values calculated from a $\underline{K}$ matrix using

MQDT. On the other hand, there are substantially more evident discrepancies between the measured and calculated β parameters than between the measured and calculated photoexcitation cross sections of these same transitions. The existence of the discrepancies provides a way of gauging the success of refinements in the calculation of the $\underline{K}$ matrix.

ACKNOWLEDGMENTS

It is a pleasure to acknowledge the $\underline{K}$ matrix and useful suggestions of C. H. Greene. This work has been supported by the U.S. Department of Energy, Office of Basic Energy Sciences.

---

*Present address: MBP Technologies, 1725 N. Service Road, Trans-Canada Highway, Dorval, Québec, Canada H9P 1J1.

[1] C. J. Dai, G. W. Schinn, and T. F. Gallagher, Phys. Rev. A **42**, 223 (1990).

[2] G. W. Schinn, C. J. Dai, and T. F. Gallagher, Phys. Rev. A **43**, 2316 (1991). [Note the matrix element $(\frac{3}{10})^{1/2}$ in Eq. (1) of Ref. [2] should be $-(\frac{3}{10})^{1/2}$, as shown in Eq. (5) of this paper. The correct value $-(\frac{3}{10})^{1/2}$ was used in all of the analyses of Ref. [2].]

[3] M. J. Seaton, Rep. Prog. Phys. **46**, 167 (1983); C. H. Greene, Phys. Rev. A **28**, 2209 (1983); J. Opt. Soc. Am. B **4**, 775 (1987).

[4] M. Aymar, J. Phys. B **20**, 6507 (1987); L. Kim and C. H. Greene, Phys. Rev. A **36**, 4272 (1987).

[5] V. Lange, U. Eichmann, and W. Sandner, J. Phys. B **22**, L245 (1989).

[6] E. Y. Xu, Y. Zhu, O. C. Mullins, and T. F. Gallagher, Phys. Rev. A **33**, 2401 (1986).

[7] Y. Zhu, E. Y. Xu, and T. F. Gallagher, Phys. Rev. A **36**, 3751 (1987); M. Aymar and J. M. Lecomte, J. Phys. B **22**, 223 (1989).

[8] C. J. Dai, S. M. Jaffe, and T. F. Gallagher, J. Opt. Soc. Am. B **6**, 1486 (1989).

[9] V. Lange, M. Aymar, U. Eichmann, and W. Sandner, J. Phys. B **24**, 91 (1991); H. Hieronymus, M. Kohl, J. Neukammer, A. König, H. Rinneberg, and H. Spinger-Bolk, Phys. Rev. A **41**, 1477 (1990); R. Kachru, N. H. Tran, P. Pillet, and T. F. Gallagher, *ibid.* **31**, 218 (1985).

[10] T. F. Gallagher, J. Opt. Soc. Am. B **4**, 794 (1987).

[11] *M.I.T. Wavelength Tables,* edited by F. M. Phelps (MIT Press, Cambridge, MA, 1982), Vol. 2, p. 3.

[12] S. A. Bhatti and W. E. Cooke, Phys. Rev. A **28**, 756 (1983); W. E. Cooke, S. A. Bhatti, and C. L. Cromer, Opt. Lett. **7**, 69 (1982).

[13] C. N. Yang, Phys. Rev. **74**, 764 (1948).

[14] C. H. Greene (private communication). See Ref. [2] for $\underline{K}$ matrix values.

[15] C. -M. Lee and K. T. Lu, Phys. Rev. A **8**, 1241 (1973); W. E. Cook and C. L. Cromer, *ibid.* **32**, 2725 (1985).

[16] D. Dill and U. Fano, Phys. Rev. Lett. **29**, 1203 (1972); D. Dill, Phys. Rev. A **6**, 160 (1972).

[17] A. R. Edmonds, *Angular Momentum in Quantum Mechanics* (Princeton University Press, Princeton, NJ, 1960), p. 107.